Science Advances

Supplementary Materials for

Laser-engineered heavy hydrocarbons: Old materials with new opportunities

X. Zang, C. Jian, S. Ingersoll, Huashan Li, J. J. Adams, Z. Lu, N. Ferralis*, J. C. Grossman*

*Corresponding author. Email: jcg@mit.edu (J.C.G.); ferralis@mit.edu (N.F.)

This PDF file includes:

Figs. S1 to S8
Tables S1 and S2
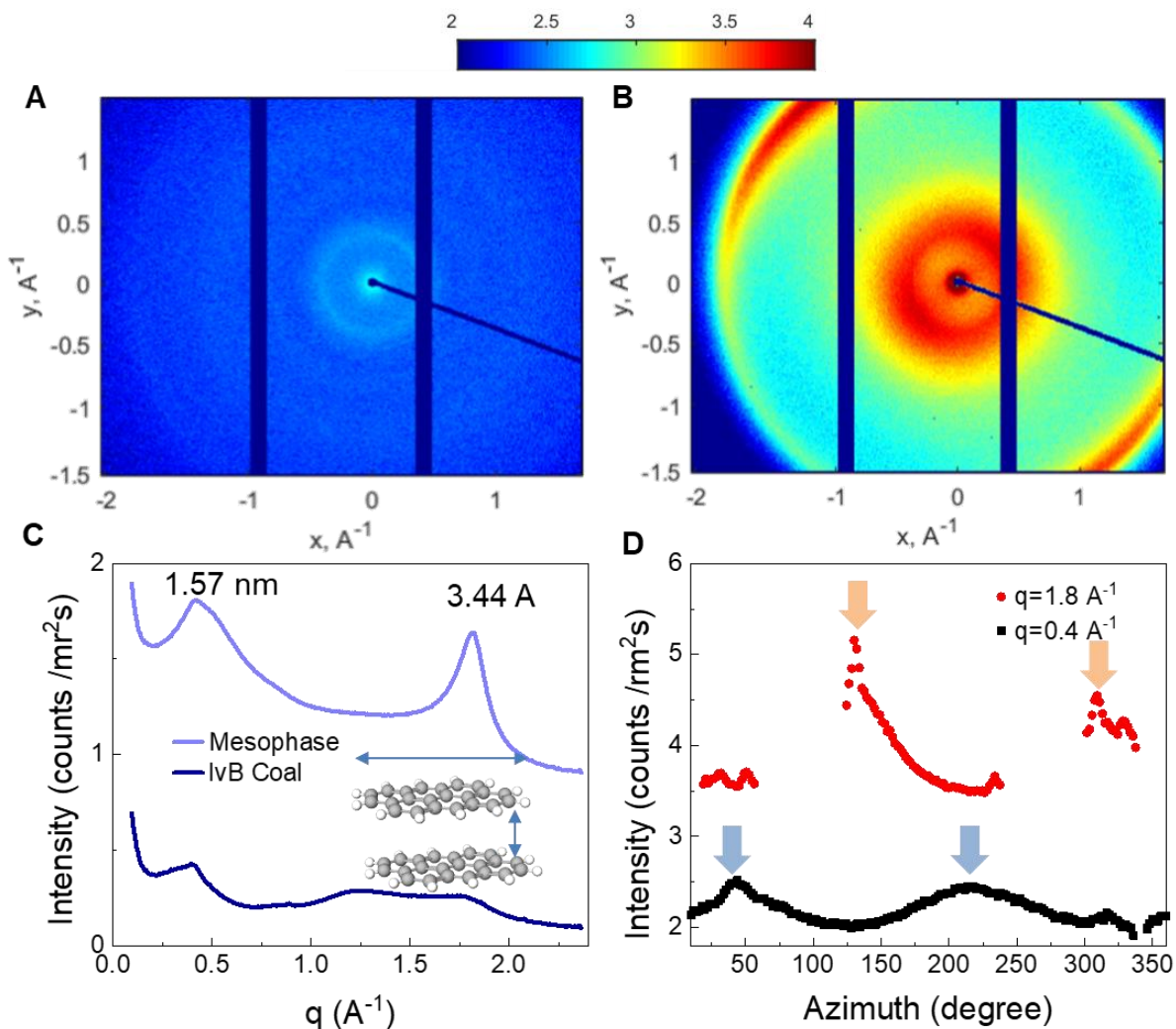
Supplementary Figures and Tables

Fig. S1. Grazing incident wide angle x-ray diffraction (GIXRD) of mesophase and coal. (A) GIXRD of lvB coal. **(B)** GIXRD of mesophase, showing obvious preferred orientation. **(C)** Integration of the diffraction patterns in (A) and (B). Mesophase shows significant peaks at q=0.4 A^{-1} and q=1.8 A^{-1}, corresponding to 1.57 nm and 3.44 A in real space. **(D)** Azimuthal projection of the two peaks in (C). The preferred orientation of two lattice space are perpendicular, indicating a stacking structure of aromatic size of ~1.57 nm with interplane distance of ~3.44 A (Fig. S1C). Such structure is consistent with reported aligned mesophase structure in references. However, the aligned polyaromatic hydrocarbon (PAH) sheets didn't yield highly graphitized conductive structure.
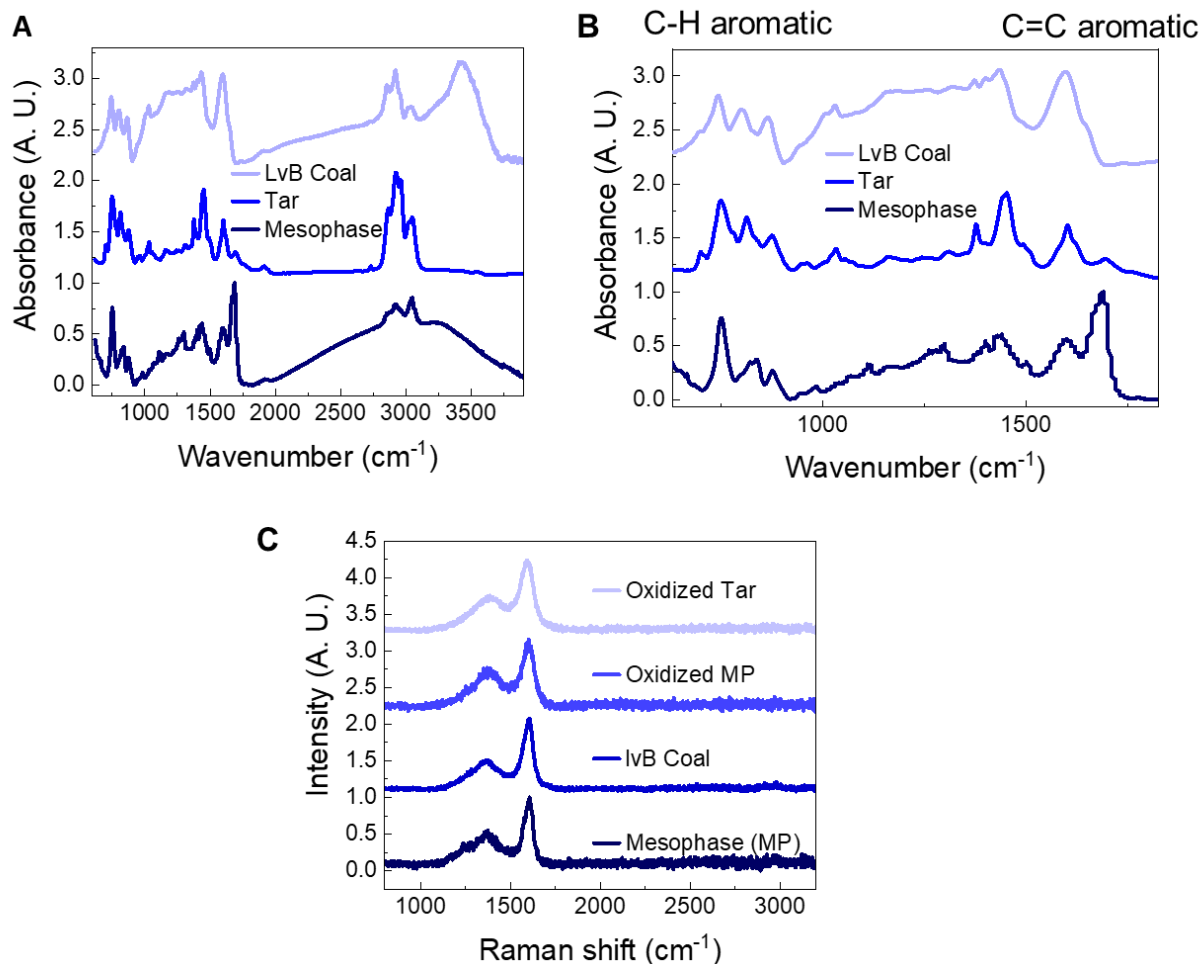
Fig. S2. Fourier transformed infrared (FTIR) and Raman spectrum of lvB coal, tar, and mesophase. (A) Full range spectrum from 400-4000 cm^{-1}. **(B)** Zoomed in spectrum near 1000 cm^{-1}. The CO_2 laser wavelength is 10.6 μm, corresponding to 940 cm^{-1}. The peaks around 940 cm^{-1} indicate bending modes of aromatic C-H which show similar finger prints on the spectrum of tar, coal and pitch. On the other hand, FTIR has strong restrictions to make quantitative conclusion. The absorption intensity is affected by the molecular orientation and film structure. The spectrum could only be used to reflect the absorption of CO_2 laser rather. It will be risky to use FTIR to calculate the absorption cross-section. **(C)** Raman spectrum of non-ablated lvB coal, mesophase, oxidized tar and mesophase. Oxygen induced crosslinking of aromatic clusters can be obtained through low temperature annealing. Without crosslinking, the small hydrocarbon aromatics in tar quench the Raman signal due to their strong fluoresce excited by the incident 472 nm laser.
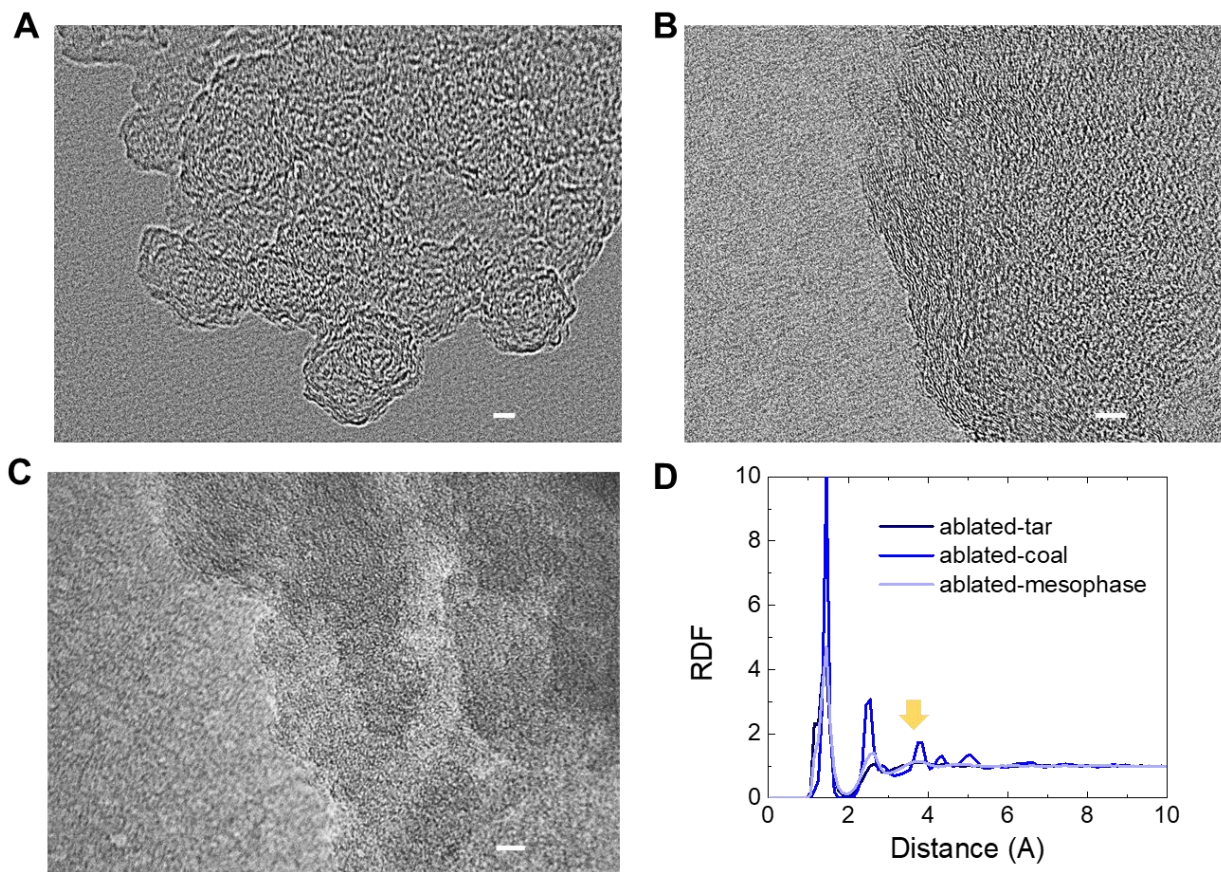
Fig. S3. Structure analysis of ablated heavy hydrocarbon. (**A-C**) Transmission electron microscopy (TEM) image of laser ablated heavy hydrocarbon. (**A**) Laser ablated steam cracked tar. (**B**) TEM image of laser ablated low volatile bituminous (LvB) coal (DECS 19). (**C**) TEM image of laser ablated mesophase pitch. Scale bar in (**A-C**) is 5 nm. Nanoscale domains of graphitic fringe stacking are observed in laser ablated tar particles, which are laterally much larger in laser ablated coal. The laser ablated mesophase are amorphous and cannot show significant contrast comparing to the carbon layer on TEM grid. (**D**) Radial distribution function of ablated tar, coal and mesophase in MD simulation. The yellow arrow point to the peak in response to the graphitic interlayer stacking. The third peak ~3.4 A is related to the graphitic stacking. Annealed coal shows sharpest RDF peaks, indicating stronger crystalline structure.

Tab. S1. Simulation set up of tar, coal, and mesophase pitch.

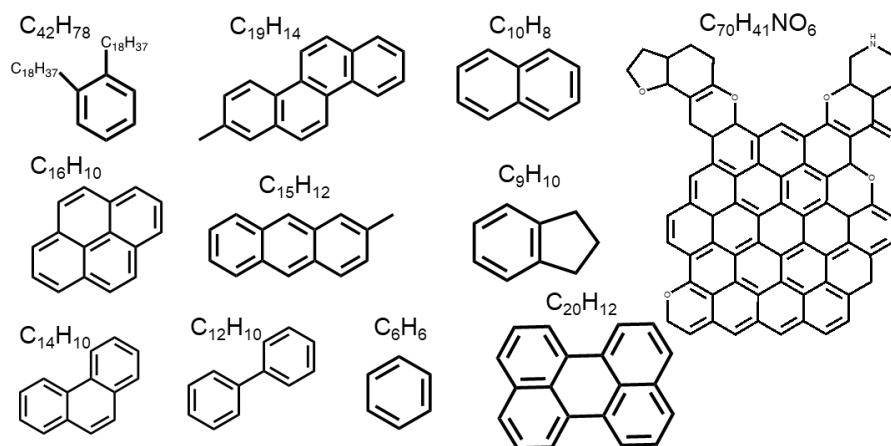| System	Chemical Formula	Number
Tar	$C_{42}H_{78}$, 1,2-dioctadecylbenzene	160
	$C_{19}H_{14}$, 2-Methylchrysene	12
	$C_{16}H_{10}$, pyrene	12
	$C_{15}H_{12}$, 2-Methylanthracene	36
	$C_{14}H_{10}$, phenanthrene	36
	$C_{12}H_{10}$, biphenyl	36
	$C_{10}H_8$, naphthalene	36
	C_9H_{10}, indane	12
	C_6H_6, benzene	12
Coal	$C_{70}H_{41}NO_6$	125
Pitch	$C_{20}H_{12}$	500

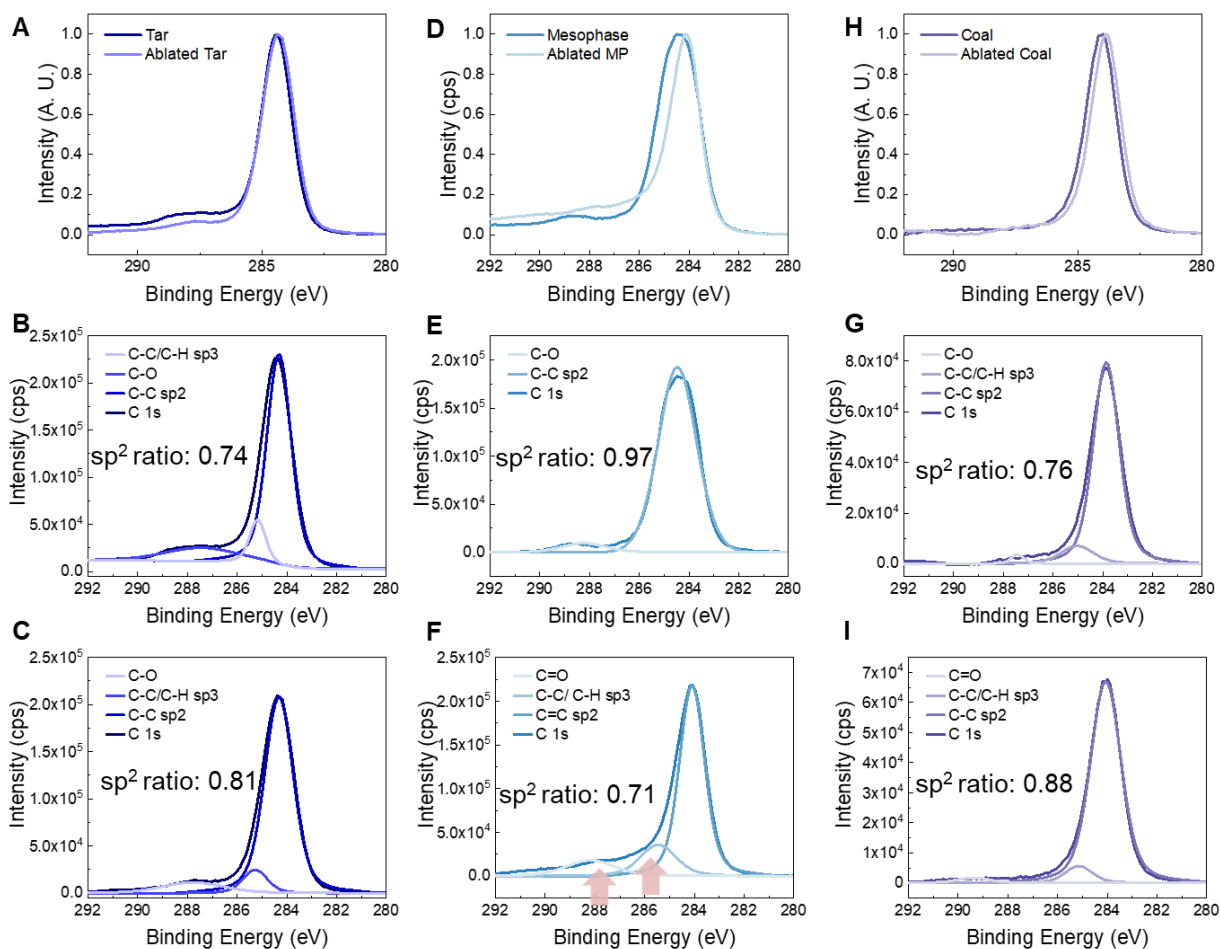**Fig. S4. Chemical Structures of molecules used in the simulation.**

Fig. S5. X-ray photoelectron spectroscopy of C 1s in nonablated and ablated tar, LvB coal, and mesophase. (**A**) Comparing C 1s spectrum of ablated and nonablated tar. (**B**) Fitted C 1s spectrum of tar. (**C**) Fitted C 1s spectrum of laser ablated tar. (**A**) Comparing C 1s spectrum of ablated and nonablated tar. (**B**) Fitted C 1s spectrum of tar. (**C**) Fitted C 1s spectrum of laser ablated tar. (**D**) Comparing C 1s spectrum of ablated and nonablated mesophase. (**E**) Fitted C 1s spectrum of mesophase. (**F**) Fitted C 1s spectrum of laser ablated mesophase. (**G**) Comparing C 1s spectrum of ablated and nonablated LvB coal. (**H**) Fitted C 1s spectrum of LvB coal. (**I**) Fitted C 1s spectrum of laser ablated LvB coal. It has to be noted that C 1s spectra of ablated tar and coal both show slighted increase of sp^2 carbon, and the symmetry of C 1s peaks retains similar to the nonablated coal and tar. However, the C 1s spectrum of ablated mesophase shows significant increase of sp^3 peak and the symmetry of C 1s peak is shifted.
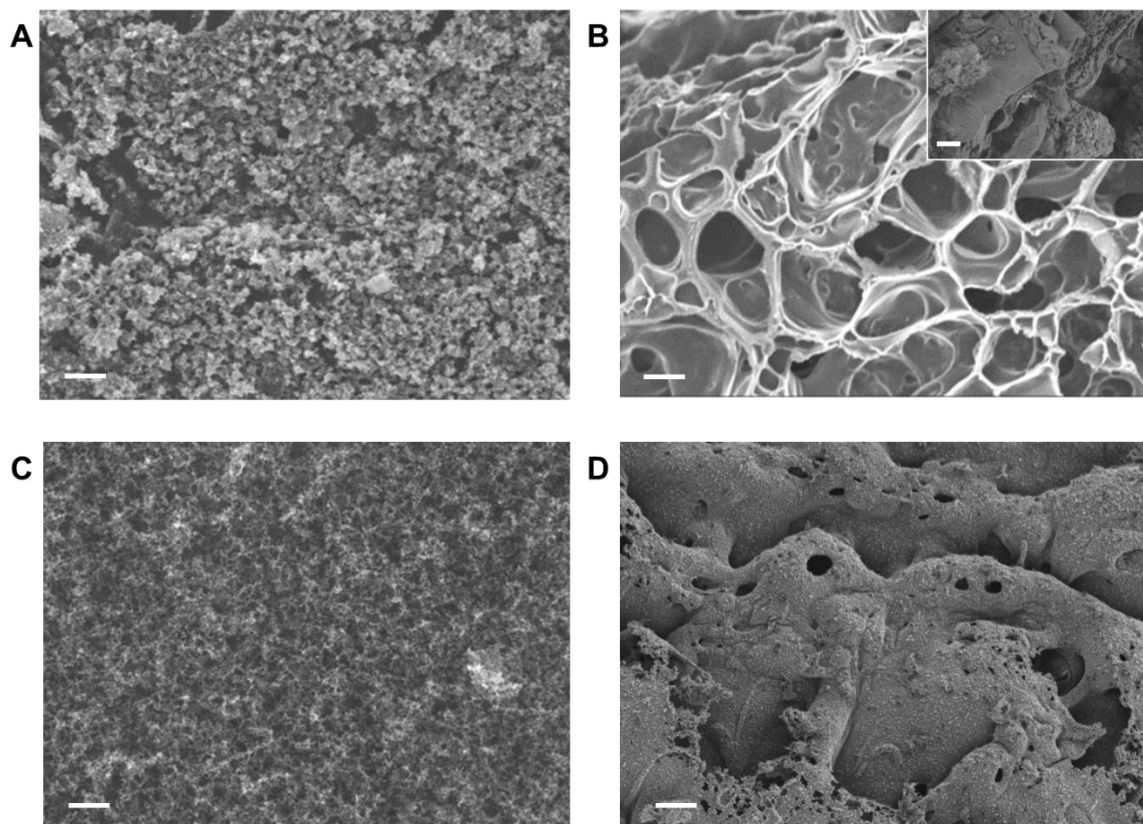
Fig. S6. SEM of laser ablated heavy hydrocarbon. (**A**) SEM image of laser ablated tar thin film. (**B**) SEM image of laser ablated LvB coal thin film. (**C**) SEM image of laser ablated mesophase pitch thin film. (**D**) SEM image of laser ablated oxidized mesophase pitch thin film. Scale bars in (**A-D**): 2 μm. Scale bar in (**B**) inset: 10 μm.

Tab. S2. Conductivity of synthetic carbon materials

| Conductivity range S/m	Carbon materials	Applications
$10^4 \sim 10^5$	CVD Graphene	FET (always-on) Transparent conductor 2D materials junctions
$10^1 \sim 10^4$	Carbon black (CB)	Low coast conductivity additive
$10^{-3} \sim 10^4$	Amorphous carbon (a-C)	Battery anodes Photovoltaic Transistor Pressure Sensor
$10^{-2} \sim 10^2$	Reduced graphene oxide R-GO	Low cost graphene altermatic
$10^{-5} \sim 10^0$	Hydrogenated amorphous carbon (a-C:H)	Conductive additive Protective coatings
$10^{-5} \sim 10^{-3}$	Tetrahedral amorphous carbon (ta-C)	Piezoelectric materials
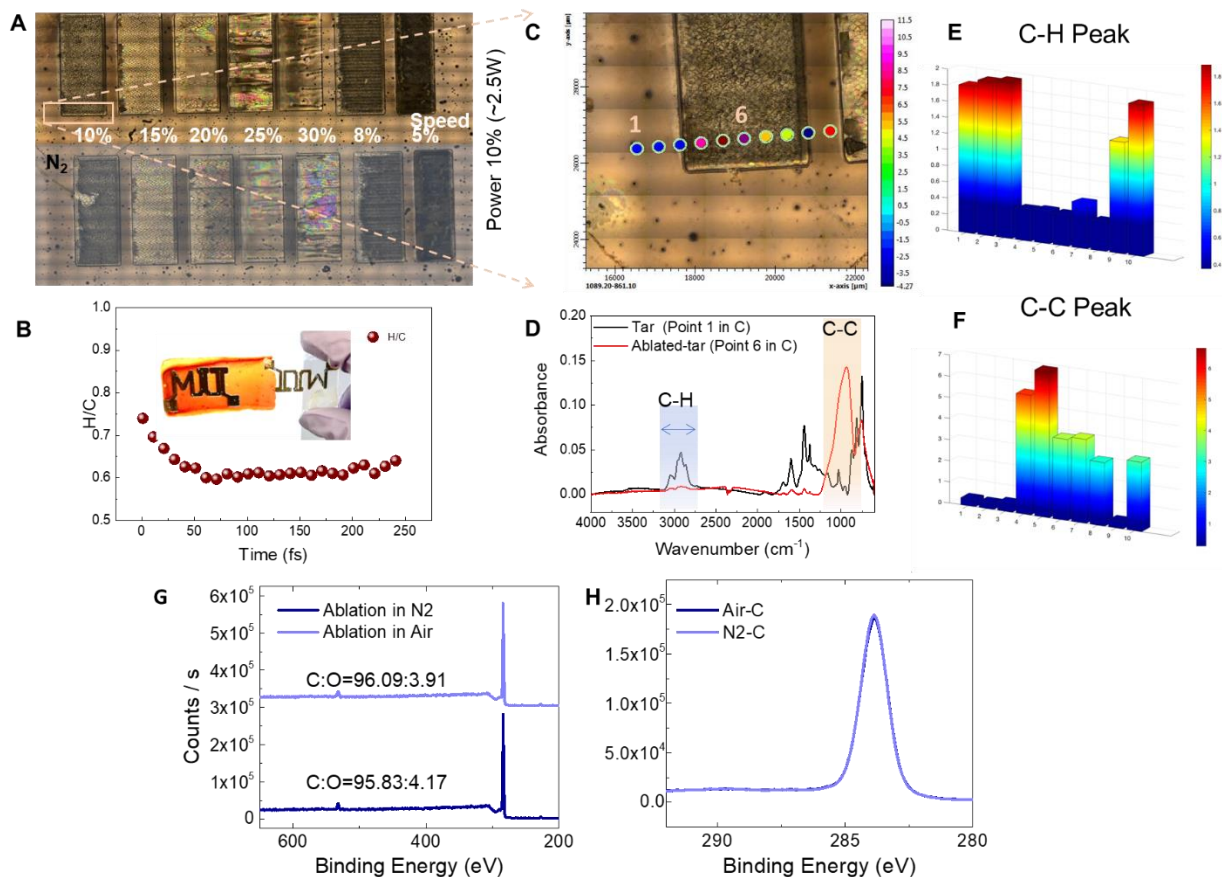
Fig. S7. Schematic of laser ablation of tar thin film. (**A**) Optical image of laser ablated area with different power, speed and defocus parameters. (**B**) Evolution of H:C ratio during the simulated laser ablation process. Inset: optical image of as receive tar and patterned MIT feature on tar thin film. Photo Credit: Xining Zang, Massachusetts Institute of Technology. (**C**) Zoomed in optical image of laser ablated tar in (**A**). Line scan of FTIR is performed along the line at the highlighted positions. (**D**) FTIR spectrum of as coated tar (in black) and laser ablated tar (in red). (**E**) Intensity of C-H peak at 3000 cm^{-1} along the scan line. (**F**) Intensity of C-H peak at 1000 cm^{-1} along the scan line. (**G**) X-ray photoelectron spectroscopy (XPS) analysis of laser ablated tar in air and nitrogen. Full range XPS spectra of laser ablated tar with and without purging nitrogen. (**H**) C 1s spectra of laser ablated tar with and without purging nitrogen, which are almost identical. Such results indicate that purging inert gas is not necessary to generate a reducing atmosphere.
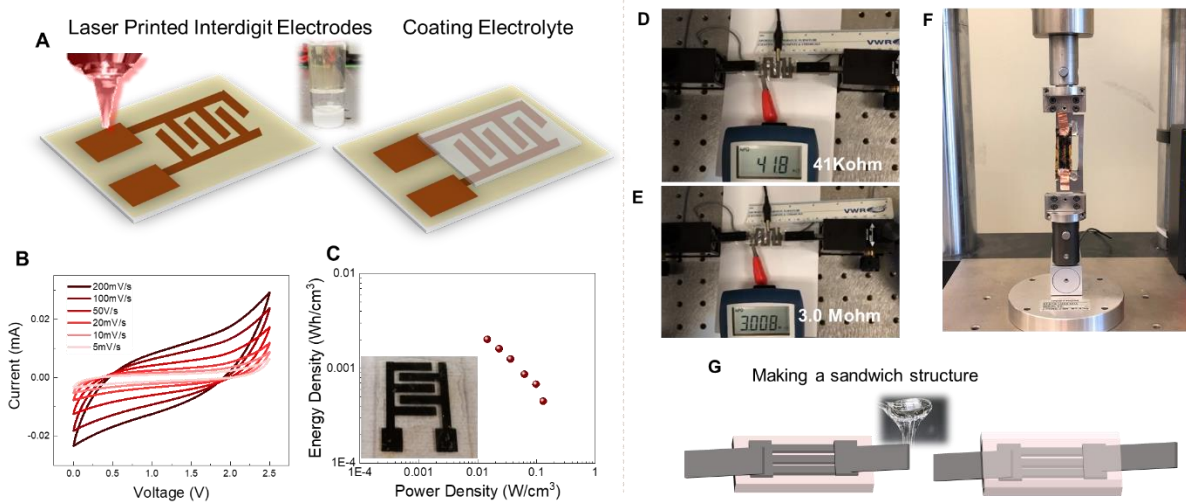
Fig. S8. Devices made from laser directed printed tar thin film. (**A**) Schematic of laser printed supercapacitor using laser ablated tar electrodes and Mg-gelatin electrolyte. (**B**) Cyclic voltammetry scanning of tar-based supercapacitor. (**C**) Specific capacitance and energy density at different scan rate derived from B. Inset: optical image of a laser printed tar-based supercapacitor. Laser printed tar shows stable cycling performance at up to 2.5 V using Mg-gelatin hydrogel electrolyte. Such high operating voltage provides a decent energy density up to 2 mWh/cm^3. The performance can be further improved by decreasing the inner resistance and optimizing the printing design. (**D-G**) Strain sensor made from laser printed tar thin film. As-ablated tar shows high gauge factor, but strong nonlinear response (**Fig. 3C**). By capping the transferred tar with another layer of PDMS, the preserved percolation shows better stability and linear response to strain (**Fig. 3B** & **Fig. 3C**). The sandwich structure of laser ablated tar-based device also provides inspirations for packing and manufacturing of other flexible and foldable devices to help improve their stability. Photo Credit: Xining Zang, Massachusetts Institute of Technology.